Journal of Power Sources 196 (2011) 76–83

Contents lists available at ScienceDirect

Journal of Power Sources

journal homepage: www.elsevier.com/locate/jpowsour

$La_{0.7}Ca_{0.3}CrO_3$–$Ce_{0.8}Gd_{0.2}O_{1.9}$ composites as symmetrical electrodes for solid-oxide fuel cells

Yingchun Zhang[a], Qingjun Zhou[a,b], Tianmin He[a,*]

[a] State Key Laboratory of Superhard Materials, College of Physics, Jilin University, Changchun 130012, PR China
[b] College of Science, Civil Aviation University of China, Tianjin 300300, PR China

ARTICLE INFO

Article history:
Received 31 May 2010
Received in revised form 8 July 2010
Accepted 9 July 2010
Available online 17 July 2010

Keywords:
Solid-oxide fuel cell
Symmetrical electrode
Electrical conductivity
Thermal expansion
Electrochemical performance
City gas

ABSTRACT

$La_{0.7}Ca_{0.3}CrO_3$ (LCC)–$Ce_{0.8}Gd_{0.2}O_{1.9}$ (GDC) composites have been investigated as symmetrical electrodes for solid-oxide fuel cells (SOFCs) on $La_{0.9}Sr_{0.1}Ga_{0.8}Mg_{0.2}O_{3-\delta}$ (LSGM) electrolyte, where there is no interlayer between anode and electrolyte. LCC oxide is chemically compatible with GDC and LSGM electrolyte at temperatures up to 1200 °C. The electrical conductivity of the LCC–GDC composites decreases with increasing GDC content. The best electrical conductivities of 18.64 S cm^{-1} in air and 1.86 S cm^{-1} in H_2 at 850 °C are achieved for an 80 wt% LCC–20 wt% GDC (LCC–GDC20) composite. The thermal expansion coefficients of the LCC–GDC composites increase with increasing GDC content, and are very close to that of the LSGM electrolyte. A cell with a 0.3 mm thick LSGM electrolyte and LCC–GDC20 symmetrical electrodes displays the highest electrochemical performance. The maximum power density is 573 mW cm^{-2} in dry H_2 and 333 mW cm^{-2} in humidified commercial city gas containing H_2S at 900 °C, respectively. These results suggest that the LCC–GDC20 composite can potentially serve as an electrode for symmetrical SOFCs operated on H_2 and commercial city gas containing H_2S.

1. Introduction

Solid-oxide fuel cells (SOFCs) are electrochemical devices that convert chemical energy directly into electrical energy with high efficiency and low pollution emissions. Therefore, SOFCs have attracted growing attention for studies on numerous types of energy generating devices [1]. An SOFC is designed as a sandwich structure of anode/electrolyte/cathode, in which porous electrodes are adhered to a dense electrolyte [2]. The anode and cathode operate separately in reducing and oxidizing environments, and hence different catalytic activities required. For both anodes and cathodes, however, some common properties are desired, such as high electronic conductivity, partial oxide ion conductivity, good electrochemical performance, and compatibility of the thermal expansion coefficient (TEC) with that of the electrolyte. Recently, it has been demonstrated that it is feasible to use the same material for both anode and cathode [3–10]. Bastidas et al. [5] investigated the use of the perovskite oxide $La_{0.75}Sr_{0.25}Cr_{0.5}Mn_{0.5}O_3$ (LSCM) as symmetrical electrodes for an LSCM/YSZ/LSCM fuel cell, and maximum power densities of 300 mW cm^{-2} and 230 mW cm^{-2} were achieved using wet H_2 and wet CH_4 at 900 °C, respectively. Jiang et al. [7] obtained 275 mW cm^{-2} and 246 mW cm^{-2} at 850 and 800 °C, respectively, under pure H_2 using an LSCM–YSZ/YSZ/LSCM–YSZ symmetrical fuel cell. The idea of symmetrical fuel cells could greatly simplify the manufacturing process [3,4]. In this way, electrodes could be dealt with under the same conditions, which would dramatically reduce the cost of fuel cell manufacture.

Unlike common single electrodes, symmetrical electrodes must simultaneously satisfy the requirements of anode and cathode. It is well known that Ni/YSZ cermet is the most commonly used anode material in SOFCs. However, this anode suffers from carbon deposition when using hydrocarbon fuels [11,12]. In a high-temperature oxidizing environment, the Ni is readily oxidized to NiO, which has little catalytic activity and significant volume expansion [13]. On the opposite side of the electrolyte, Sr-doped $LaMnO_3$ (LSM) is the typical cathode material for SOFCs. However, an LSM cathode is unstable in a reducing atmosphere [14,15]. Therefore, as mentioned above, the conventional electrodes are not suitable for use as symmetrical electrodes due to their various defects. It is highly desirable to develop new symmetrical electrodes for application in SOFCs.

$LaCrO_3$-based perovskite oxides have been investigated as alternative anode materials for application in hydrocarbon-fueled SOFCs due to their low activity towards carbon deposition [16]. It has been reported that the product of substitution of the A-site in $LaCrO_3$ by Ca showed catalytic activity for CH_4 and had low activity toward carbon deposition [17]. Recently, $La_{0.7}Ca_{0.3}CrO_3$ (LCC) perovskite oxide has been demonstrated to be potentially useful as a cathode material for SOFCs [18]. However, $LaCrO_3$-based anodes generally show poor catalytic activity for anode oxidation reac-

* Corresponding author. Tel.: +86 431 88499039; fax: +86 431 88498000.
E-mail addresses: hly@mail.jlu.edu.cn, hetm@jlu.edu.cn (T. He).

0378-7753/$ – see front matter © 2010 Elsevier B.V. All rights reserved.
doi:10.1016/j.jpowsour.2010.07.035

tions, low ionic conductivity under anodic conditions, and weak adherence to solid electrolytes [19]. In order to improve the performances of such anodes, one of the effective ways is to introduce an electrolyte component into the anode to form a composite anode [20–22], the electrochemical activity of which could be enhanced by increasing the number of triple-phase boundary sites. In addition, the introduction of electrolyte forms a mixed ionic–electronic conductor, such that the oxygen ionic conductivity of the anodes will be significantly enhanced. Moreover, the thermal expansion compatibility of the anode with the electrolyte might also be improved. The advantage of this type of composite material is that the reaction region will be extended from the interface between electrode and electrolyte to the overall electrode [23]. It was noted that, for a $LaGaO_3$-based SOFC, an interlayer had to be introduced at the anode/electrolyte interface to prevent the interfacial reaction when using a nickel-containing anode [24,25]. However, the inclusion of the interlayer will undoubtedly increase the interfacial resistance and the difficulty of fabrication. In this regard, the development of alternative anode materials is needed to eliminate the interlayer limitation.

In the work described in this paper, $La_{0.7}Ca_{0.3}CrO_3$ (LCC)–$Ce_{0.8}Gd_{0.2}O_{1.9}$ (GDC) composites have been investigated as symmetrical electrodes for use in SOFCs on $La_{0.9}Sr_{0.1}Ga_{0.8}Mg_{0.2}O_{3-\delta}$ (LSGM) electrolyte without using an interlayer at the anode/electrolyte interface. The feasibility of LCC–GDC composites as symmetrical electrodes has been assessed in detail, including with regard to electrical conductivity, chemical compatibility, TEC, and electrochemical performance. The single-cell performances of LCC–GDC symmetrical electrodes have also been tested under dry H_2 and humidified commercial city gas containing H_2S (3% H_2O).

2. Experimental

2.1. Preparation of samples and symmetrical fuel cells

$La_{0.9}Sr_{0.1}Ga_{0.8}Mg_{0.2}O_{3-\delta}$ (LSGM) powder was synthesized by the glycine–nitrate process (GNP) [26]. Dense LSGM pellets of 13 mm in diameter were prepared by uniaxial pressing of LSGM powder at 220 MPa and subsequently sintering at 1450 °C for 10 h in air. LSGM electrolyte substrates with a fixed thickness of 0.3 mm were obtained by wet grinding of the sintered pellets with waterproof abrasive paper.

$La_{0.7}Ca_{0.3}CrO_3$ (LCC) and $Ce_{0.8}Gd_{0.2}O_{1.9}$ (GDC) were also synthesized by the GNP. Stoichiometric amounts of $La(NO_3)_3{\cdot}6H_2O$, $Ca(NO_3)_2{\cdot}4H_2O$, and $Cr(NO_3)_3{\cdot}9H_2O$ were dissolved in deionized water. Glycine was added in a 1.57:1 molar ratio of glycine to nitrate. Similarly, stoichiometric amounts of $Ce(NO_3)_3{\cdot}6H_2O$ and Gd_2O_3 were dissolved in nitric acid and 1 mol of glycine was added per mole of nitrate. The mixtures were heated until spontaneous combustion occurred to afford the precursors. The precursor powder was ground in an agate mortar for 30 min. The LCC precursor was then calcined at 1100 °C for 10 h, while the GDC precursor was calcined at 650 °C for 2 h to remove residual organic matter and to ensure a single-phase composition. The mixture of the calcined LCC and GDC powders was ground with ethanol for 2 h to form composites with 20, 30, and 40 wt% GDC (hereinafter referred to as LCC–GDC20, LCC–GDC30, and LCC–GDC40). The well-mixed composites were uniaxially pressed into pellets (Φ13 mm × (0.7 ± 0.1) mm) at 220 MPa and cylinders (Φ6 mm × (6 ± 0.2) mm) at 170 MPa for electrical conductivity and thermal expansion measurements. The pellets and cylinders were subsequently sintered at 1200 °C for 2 h in air at a heating rate of 2 °C min^{-1}. For cell fabrication, a composite electrode slurry was prepared by mixing the composites with the binder. The slurry of LCC–GDC composite electrode material was then screen-painted on either side of the LSGM pellets. After drying, the electrodes were sintered at 1200 °C for 2 h in air at a heating rate of 2 °C min^{-1}. Silver paste was painted onto both electrodes as current collector and baked at 110 °C for 1 h. The LSGM electrolyte pellet was sealed onto an alumina tube with silver paste to make a single symmetrical cell.

2.2. Characterization

The phase composition of the synthesized powders and the chemical compatibility between LCC, GDC, and LSGM were assessed by X-ray diffraction (XRD) analysis on an X-ray diffractometer (Rigaku-D-Max γA system; Cu-K_α radiation, λ = 0.15418 nm), with a step size of 0.02° and a scanning range of 20–80° at room temperature. Electrical conductivity measurements were performed by the van der Pauw method over the temperature range from 300 to 850 °C in air and H_2 environments. TECs of samples were measured using a dilatometer (Netzsch DIL 402C) with an Al_2O_3 reference over the range from 30 to 1000 °C. A heating rate of 5 °C min^{-1} and an air flow rate of 60 mL min^{-1} were adopted during these measurements. Single-cell performances of the symmetrical electrodes were tested using an electrochemical workstation (CHI604C) with dry hydrogen and humidified commercial city gas containing H_2S (3% H_2O) as fuels and ambient air as oxidant at various temperatures. Microstructures of the electrodes exposed to H_2 and commercial city gas were observed after cell testing with scanning electron microscopy (SEM) (JEOL JSM-6480LV). Elemental analyses were determined with energy dispersive X-ray spectroscopy (EDS, EDAX CDU) by EDAX ZAF Quantification [27].

3. Results and discussion

3.1. XRD analysis

Fig. 1(a) and (b) shows the XRD patterns of LCC and GDC powders calcined at 1100 °C for 10 h and at 650 °C for 2 h, respectively. The samples of nominal composition LCC and GDC were confirmed to be single phases by XRD, i.e., the single-phase LCC and GDC oxides had an orthorhombic perovskite and a cubic fluorite structure, respectively. For composite electrodes, the phase reaction between the electrode components is generally deleterious for practical application in SOFCs. To evaluate the chemical compatibility between LCC and GDC, the phase reaction of LCC with electrolytes with different GDC contents was investigated by sintering mixtures of

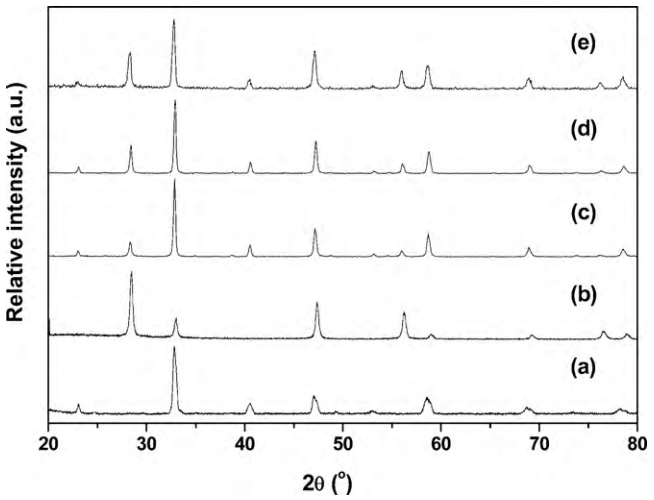

Fig. 1. XRD patterns of (a) LCC powders calcined at 1100 °C for 10 h, (b) GDC powders calcined at 650 °C for 2 h, (c) LCC–GDC20 powders, (d) LCC–GDC30 powders, and (e) LCC–GDC40 powders sintered at 1200 °C for 2 h.

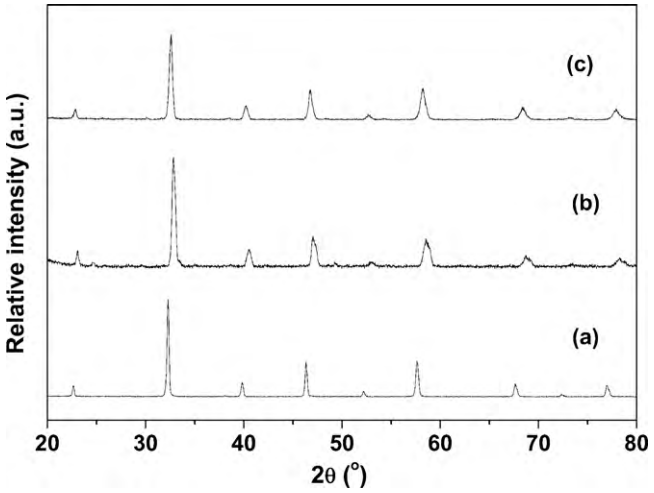

Fig. 2. XRD patterns of (a) LSGM powders sintered at 1450 °C for 10 h, (b) LCC powders calcined at 1100 °C for 10 h, and (c) LCC–LSGM powders sintered at 1200 °C for 2 h.

the two powders. Fig. 1(c)–(e) shows the XRD patterns of the LCC–GDC20/30/40 composite powders sintered at 1200 °C for 2 h. As can be seen, the LCC–GDC20/30/40 composite oxides were physical mixtures of LCC and GDC oxides. No impurity peaks and no shifts of the XRD peaks in the patterns were detected. This indicated that there was no chemical reaction between the LCC and GDC oxides under sintering at 1200 °C for 2 h, regardless of the GDC content in this range, suggesting that the LCC material had good chemical compatibility with the GDC electrolyte. This result is in good agreement with that reported previously in a study of LCC and $ReO_{1.5}$-doped CeO_2 composite interconnections [28,29]. The chemical compatibility between LCC and LSGM was also evaluated by sintering mixtures of the two powders in a weight ratio of 1:1, and the resultant XRD patterns are shown in Fig. 2. Evidently, there was no significant reaction between LCC and LSGM. This indicates that LCC is chemically compatible with LSGM electrolyte.

3.2. Electrical conductivity

The overall conductivities of the LCC–GDC composites were determined by the van der Pauw method in the temperature range 300–850 °C in air and in H_2. Fig. 3 shows the temperature dependences of the electrical conductivities of LCC–GDC samples with different GDC contents measured in air. The electrical conductivity of each LCC–GDC sample gradually increased with increasing temperature, corresponding to semiconductor-like behavior. Similar behavior has been described for undoped and doped $LaCrO_3$ oxides as p-type semiconductors [18,29,31,32], in which the electronic conduction in the samples proceeds by the small-polaron mechanism through the transport of electron holes. Meanwhile, GDC is an ionic conductor, in which oxygen ion conduction is achieved through the hopping of oxygen vacancies [20,33]. The oxygen ionic conductivity of GDC is obviously lower than the electronic conductivity of LCC [34]. Therefore, the overall conductivity of LCC–GDC composites is dominated by the LCC electronic conductivity. No conduction mechanism transformation was detected in the temperature range from 300 to 850 °C. Arrhenius plots displayed a strictly linear relationship, indicating a small-polaron thermally activated mechanism. The electrical conductivity behavior obeyed the following equation:

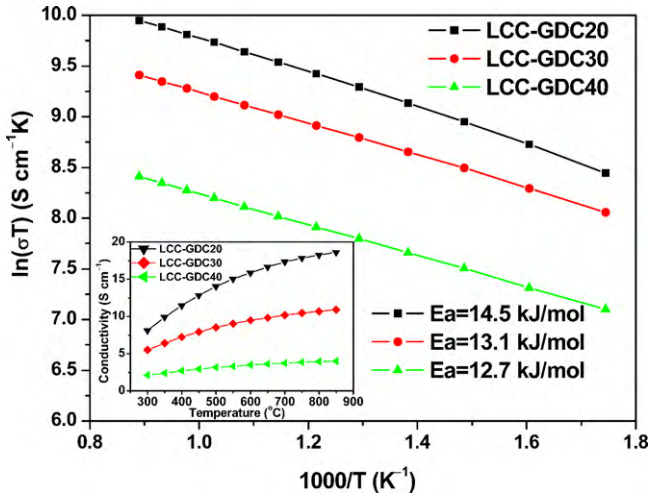

Fig. 3. Temperature dependence of the electrical conductivity of the LCC–GDC samples with different GDC contents in air.

$$\sigma = \frac{A}{T}\ \exp\left(-\frac{Ea}{kT}\right) \quad (1)$$

where A is the pre-exponential constant, k is the Boltzmann constant, T is the absolute temperature, and Ea is activation energy of the electrical conductivity. The activation energy Ea was calculated from the slope of the curve of $\ln(\sigma T)$ *vs* $1000/T$, as shown in Fig. 3, which yielded values of 14.5, 13.1, and 12.7 kJ mol^{-1} for the LCC–GDC20, LCC–GDC30, and LCC–GDC40 samples, respectively, in the temperature range 300–850 °C. The activation energy, Ea, of the electrical conductivity for undoped and doped $LaCrO_3$ has been reported to be in the range 10–20 kJ mol^{-1} [18]. The data obtained in this study fall within this reported range. In addition, the electrical conductivities of the LCC–GDC composites decreased with increasing GDC content. As stated above, the conductivity of the LCC–GDC composites could be mainly attributed to the LCC electronic conductivity. GDC seemed to act just like an insulator in the composites. Addition of the GDC phase destroyed the consecutive LCC electronic conductive phase. Thus, the more GDC was added, the lower the electrical conductivity became. Among the studied compositions, the LCC–GDC20 sample exhibited the best electrical conductivity of 18.6 S cm^{-1} at 850 °C in air.

For LCC–GDC composites, the respective contributions of LCC and GDC were responsible for the electrical conductivity behavior. We will discuss the contributions of LCC to the electrical conductivity behavior. The contribution of GDC will be discussed in detail in the following paragraphs. Fig. 4 shows the temperature dependences of the electrical conductivities of LCC–GDC samples with different GDC contents measured in H_2 (100 mL min^{-1}). It can be seen from Fig. 4 that the electrical conductivity of each LCC–GDC sample was significantly reduced in H_2 as compared to the value in air. This was mainly due to the reduction of Cr^{4+} to Cr^{3+} accompanying the formation of an oxygen vacancy (δ). The electroneutrality relationship for calcium-doped lanthanum chromites can be expressed by Eq. (2) [29]:

$$La_{1-x}Ca_x(Cr^{3+})_{1-x}(Cr^{4+})_xO_3 \leftrightarrow La_{1-x}Ca_x(Cr^{3+})_{1-x+2\delta}(Cr^{4+})_{x-2\delta}O_{3-\delta} + \left(\frac{\delta}{2}\right)O_2(g) \quad (2)$$

This process is highly sensitive to the temperature and oxygen partial pressure [29,35]. Similar to the trends in the conductivity behavior seen in air, the electrical conductivity decreased in H_2 with increasing GDC content. The LCC–GDC20 sample displayed the highest electrical conductivity of 1.86 S cm^{-1} at 850 °C in H_2. The plots of $\ln(\sigma T)$ *vs* $1/T$ in Fig. 4 clearly do not show a linear relationship in the investigated temperature range. Instead, the electrical conductivity behavior has two components, i.e., there are two dif-

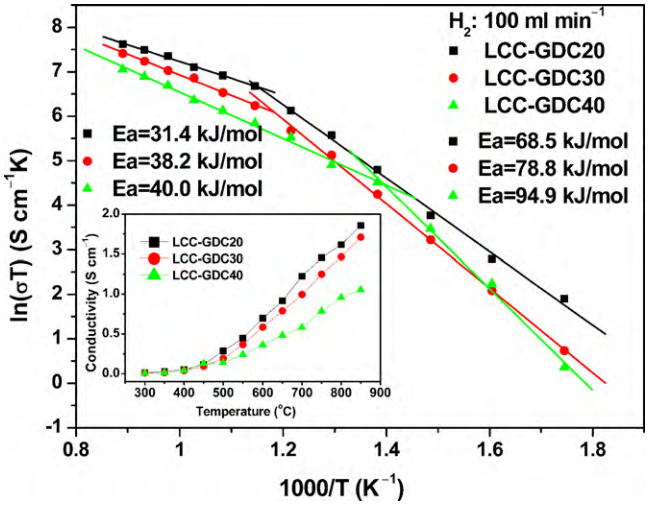

Fig. 4. Temperature dependence of the electrical conductivity of the LCC–GDC samples with different GDC contents in H_2.

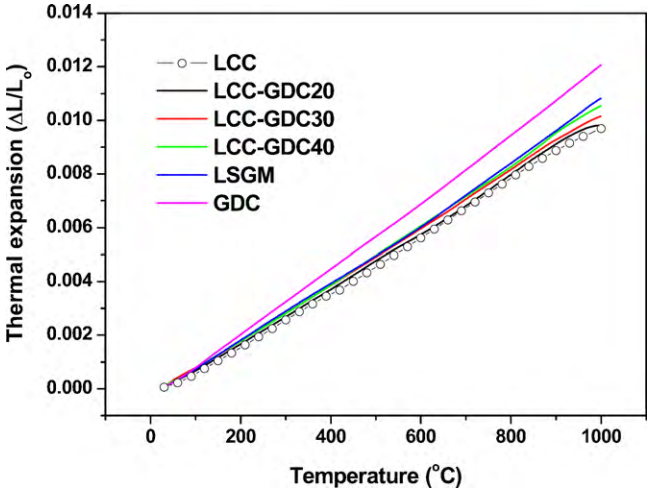

Fig. 5. Thermal expansion curves of LCC–GDC composites and the selected materials over temperature range 30–1000 °C in air.

ferent linear Arrhenius electrical conductivity behaviors in the high- and low-temperature ranges, which correspond to the change in the oxygen vacancy and electron hole concentrations. For the LCC–GDC20/30 samples, Arrhenius electrical conductivity behavior with curvature appeared at around 600 °C. For the LCC–GDC40 sample, however, curvature of the Arrhenius electrical conductivity behavior appeared at around 450 °C. At temperatures higher than 600 °C for LCC–GDC20/30 and 450 °C for LCC–GDC40, the slopes of the electrical conductivity behavior were reduced compared to those in the low-temperature range, which meant that the activation energies of the samples diminished at temperatures above 600 (or 450) °C. The different electrical conductivities in air and in H_2 can be attributed to different compensation mechanisms, i.e., electronic hole and oxygen vacancy compensation. This indicated that the conduction activation energy was also different. The specific data for the conduction activation energy are shown in Fig. 4. It is well known that for $LaCrO_3$-based perovskite oxides there is a non-stoichiometry at the oxygen sites at low oxygen partial pressures of 10^{-8}–10^{-18} atm [36,37]. Under a reducing atmosphere, charge compensation through Cr^{4+} being reduced to Cr^{3+} occurs by the formation of oxygen vacancies as described in Eq. (3), according to the defect reaction written in the Kröger–Vink notation:

$$2Cr_{Cr}^{\bullet} + O_O^{\times} \leftrightarrow 2Cr_{Cr}^{\times} + V_O^{\bullet\bullet} + \frac{1}{2}O_2(g) \quad (3)$$

where $Cr_{Cr}^{\bullet}$ is a Cr^{4+} ion at the Cr-site in the LCC, $Cr_{Cr}^{\times}$ is a Cr^{3+} ion at the Cr-site, $O_O^{\times}$ is an O^{2-} ion in the lattice, and $V_O^{\bullet\bullet}$ is an oxygen vacancy in the lattice. As mentioned above, $LaCrO_3$-based oxide is a p-type semiconductor, in which electrical conduction is mainly mediated by a small-polaron hopping mechanism along the Cr^{4+}–O^{2-}–Cr^{3+} network. The electrical conduction of LCC proceeds through the transport of electron holes localized at Cr sites (i.e., $Cr_{Cr}^{\bullet}$) [38]. The formation of oxygen vacancies in a reducing atmosphere simultaneously decreases the concentration of $Cr_{Cr}^{\bullet}$, thus resulting in a reduction in the electrical conductivity as the concentration of small polarons is decreased. The curvature of the Arrhenius electrical conductivity behavior at around 600 (or 450) °C for LCC–GDC20/30 and LCC–GDC40 can thus be partially attributed to an order–disorder transition of the oxygen vacancies. This is supported by the chemical diffusion coefficient results for Ca-doped $LaCrO_3$ reported by Yasuda and Hishinuma [39], which confirmed that the oxygen vacancies were randomly distributed. A similar curvature of the Arrhenius electrical conductivity behavior in H_2 has also been reported by another author in relation to $La_{0.7}Ca_{0.3}Cr_{0.95}Zn_{0.05}O_{3-\delta}$ interconnect ing material [40].

As noted above, two factors are expected to contribute to the electrical conductivity behavior in LCC–GDC composites, although that of LCC makes the major contribution. The other contribution to the electrical conductivity behavior for LCC–GDC composites comes from the GDC. Under a reducing atmosphere at high temperature, GDC is a mixed ionic–electronic conductor due to the presence of some electronic conductivity through reduction of Ce^{4+} to Ce^{3+} [34]. The electroneutrality relationship can be written as:

$$2Ce_{Ce}^{\times} + O_O^{\times} \leftrightarrow 2Ce_{Ce}' + V_O^{\bullet\bullet} + \frac{1}{2}O_2(g) \quad (4)$$

where $Ce_{Ce}^{\times}$ is a Ce^{4+} ion in a Ce-site in GDC, and Ce_{Ce}' is a Ce^{3+} ion in a Ce-site. Therefore, the increase in the electrical conductivity of the samples in the high-temperature range stemmed partially from the contribution of the GDC. Previous investigations have demonstrated that curvature of plots of $\ln(\sigma T)$ *vs* $1/T$ for GDC appears at around 585 °C under reducing conductions, whereupon short-range order appears among the disordered vacancies [41]. The presence of short-range order increases the effective *Ea*, thus leading to curvature in the plots of $\ln(\sigma T)$ *vs* $1/T$ above the stated temperatures for LCC–GDC. Steele [42] reported that the conductivity behavior of a GDC sample displayed a curvature at 450 °C, above which temperature the $(Gd_{Ce}' - V_O^{\bullet\bullet})$ defect complex was essentially dissociated, while below it the defect complex was trapped. On increasing the GDC content from 20% to 40%, the curvature temperature of the plots of $\ln(\sigma T)$ *vs* $1/T$ decreased from 600 to 450 °C. This was probably due to the conductivity behavior of GDC component, which became increasingly significant with increasing GDC content.

3.3. Thermal expansion behavior

The TECs of the electrolyte and electrode should be as similar as possible so as to minimize thermal stresses between the cell components. The linear TECs of the LCC–GDC composites were determined by means of a dilatometer over the temperature range 30–1000 °C. Fig. 5 shows the thermal expansion curves of the LCC–GDC composites in the temperature range 30–1000 °C in air. For comparison, the thermal expansion curves of the LCC, LSGM, and GDC materials are also shown in Fig. 5. The specific linear TECs of the samples are listed in Table 1. The TECs of the LCC–GDC composites are seen to increase with increasing GDC content. The TECs of the LCC and GDC samples were determined as $9.93 \times 10^{-6}\,K^{-1}$

Table 1
Average thermal expansion coefficients of the LCC–GDC composites and the selected materials between 30 and 1000 °C in air.

Sample	TEC ($\times 10^{-6}$ K^{-1})
LCC	9.93
LCC–GDC20	10.1
LCC–GDC30	10.4
LCC–GDC40	10.8
LSGM	11.5
GDC	12.4

(Mori et al. [30] reported a value of 9.7×10^{-6} K^{-1} between 50 and 1000 °C) and 12.4×10^{-6} K^{-1}, respectively, in the temperature range 30–1000 °C in air. The upward trend in the TECs in LCC–GDC composites of 10.1×10^{-6} K^{-1} to 10.8×10^{-6} K^{-1} with increasing GDC content can be attributed to the higher TEC of GDC. It can be seen from Table 1 and Fig. 5 that the TECs of the LCC–GDC samples were close to that of the LSGM electrolyte (11.5×10^{-6} K^{-1}), showing good TEC compatibility between the two materials. As shown in Fig. 5, there was no curvature in the thermal expansion plots, suggesting that no structural transformation occurred in the LCC–GDC composites in the measured temperature range.

3.4. Electrochemical performance

The *I–V* and *I–P* characteristics of the LCC–GDC/LSGM/LCC–GDC symmetrical cells were tested under dry H_2 and humidified commercial city gas containing H_2S (3% H_2O) fuels with ambient air as oxidant at different temperatures. For H_2 fuel, a flow rate of 100 mL min^{-1} was adopted, while for humidified commercial city gas (3% H_2O) fuel the flow rate was 50 mL min^{-1}. The composition of the commercial city gas and the concentration of impurity gases therein have been described previously [43]. The basis of the city gas is hydrogen (59.6%), methane (22.1%), carbon monoxide (9.3%), and nitrogen (3.4%), and the main impurities are ammonia (~12 ppm) and H_2S (~5 ppm). Table 2 shows the maximum power densities of symmetrical fuel cells with various configurations. Fig. 6(a)–(c) shows cell voltage and power density as a function of current density for LCC–GDC/LSGM/LCC–GDC symmetrical cells with different GDC contents. As can be seen, the performances of the symmetrical cells were enhanced with increasing temperature. The LCC–GDC20/LSGM/LCC–GDC20 cell always occupied the top position, with maximum power densities of 387 and 573 mW cm^{-2} at 850 and 900 °C, respectively. This result was consistent with the electrical conductivities of the LCC–GDC composites. The performances of the cells with composite electrodes generally decreased in the order: LCC–GDC20 > LCC–GDC30 > LCC–GDC40. The decrease in cell performance with increasing GDC content can be attributed to the decrease in electrical conductivity. The open-circuit voltage for the LCC–GDC20/LSGM/LCC–GDC20 cell was slightly lower than those for the other cells. This may have been a result of gas leakage from the cell seal. The cell performance might have been further enhanced by improving the cell seal. Therefore, from a comprehensive review of its performance, we conclude that the LCC–GDC20/LSGM/LCC–GDC20 cell shows excellent prospects. To examine the anode performance in a complex hydrocarbon fuel, the symmetrical cell performance was tested in commercial city gas containing H_2S (3% H_2O). Fig. 7 shows cell voltage and power density as a function of current density for the LCC–GDC/LSGM/LCC–GDC symmetrical cell measured when using humidified commercial city gas containing H_2S (3% H_2O) as fuel and ambient air as oxidant at different temperatures. The maximum power densities of the cells were 333, 285, and 280 mW cm^{-2} at 900 °C for GDC contents of 20%, 30%, and 40%, respectively. The *I–V* and *I–P* curves of the LCC–GDC30/LSGM/LCC–GDC30 cell

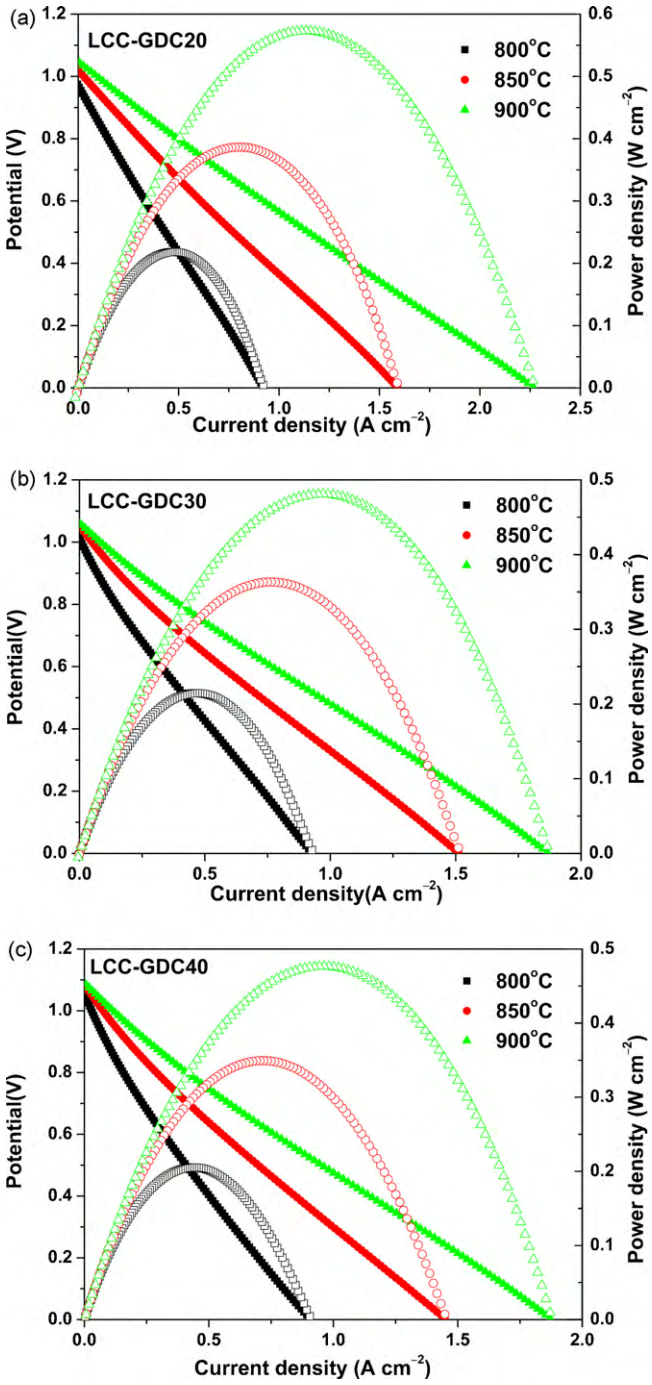

Fig. 6. Electrochemical performance data of the LCC–GDC/LSGM/LCC–GDC symmetrical cells using dry H_2 as fuel and ambient air as oxidant in the temperature range from 800 to 900 °C for various GDC contents: (a) 20%, (b) 30%, and (c) 40%.

are not shown in Fig. 7 because of their similarity to those of the LCC–GDC40/LSGM/LCC–GDC40 cell, for example, the maximum power density of 285 mW cm^{-2} at 900 °C. To examine the stability of the LCC–GDC20 anode, a potentiostatic test was carried out in commercial city gas containing H_2S for 20 h. Fig. 8 shows the electrochemical stability of the LCC–GDC20/LSGM/LCC–GDC20 cell measured using humidified commercial city gas containing H_2S (3% H_2O) as fuel over a test period of 20 h. The current density of the cell decreased significantly in the first 0.5 h due to the fuel switching from H_2 to city gas. The system subsequently entered into a relatively stable state, after which there was only a small decrease in the ensuing 19.5 h, suggesting that the LCC–GDC20 composite

Table 2
Summary of maximum power densities of some symmetrical cells with different electrodes and electrolytes under various fuel conditions.

Cathode/electrolyte/anode	Thickness of electrolyte (mm)	Temperature (°C)	P_{max} (mW cm^{-2})				Ref.
			H_2	5%H_2	CH_4	City gas	
LSCM–(50% YSZ:50% CGO)/YSZ/LSCM–(50% YSZ:50% CGO)	0.18	950	400		~120		[3]
YSZ–CeO_2(1:1)/YSZ/YSZ–CeO_2(1:1)	1.21	950	140		<50		[4]
LSCM/YSZ/LSCM	0.2	900	300	170	230		[5]
LSCM/YSZ/LSCM	0.25	950	546	326	347		[6]
LSCM–YSZ/YSZ/LSCM–YSZ	0.05	850	275				[7]
		800	246				
LSSM/ScSZ/LSSM	0.3	900	310		130		[8]
		850	220		100		
LCC/YSZ/LCC	1–2	950	110		25		[9]
LSTF/YSZ/LSTF	1–2	950	100		~40		
LCC–YSZ(1:1)/YSZ/LCC–YSZ(1:1)	2	950	110		<30		[10]
LSTF60:YSZ:CeO_2/YSZ/LSTF60:YSZ:CeO_2	1	950	<100	<40	~40		[46]
LCC–YSZ(1:1)/YSZ/LCC–YSZ(1:1)	0.35	850	92.1				[47]
PCCM/YSZ/PCCM	0.37	950	250	<150	160		[48]
LCC–GDC20/LSGM/LCC–GDC20	0.3	900	573			333	This work
LCC–GDC30/LSGM/LCC–GDC40	0.3	900	481			285	
LCC–GDC40/LSGM/LCC–GDC40	0.3	900	476			280	

LSCM: $(La_{0.75}Sr_{0.25})Cr_{0.5}Mn_{0.5}O_{3-\delta}$; CGO(GDC): $Ce_{0.8}Gd_{0.2}O_{2-\delta}$; LSSM: $La_{0.8}Sr_{0.2}Sc_{0.2}Mn_{0.8}O_3$; ScSZ: $(Sc_2O_3)_{0.1}(ZrO_2)_{0.9}$; LCC: $La_{0.7}Ca_{0.3}CrO_{3-\delta}$; LSTF: $La_4Sr_8Ti_{12-x}Fe_xO_{38-\delta}$; LSGM: $La_{0.9}Sr_{0.1}Ga_{0.8}Mg_{0.2}O_{3-\delta}$; LSTF60: $La_4Sr_8Ti_6Fe_6O_{38-\delta}$; PCCM: $Pr_{0.7}Ca_{0.3}Cr_{0.6}Mn_{0.4}O_{3-\delta}$.

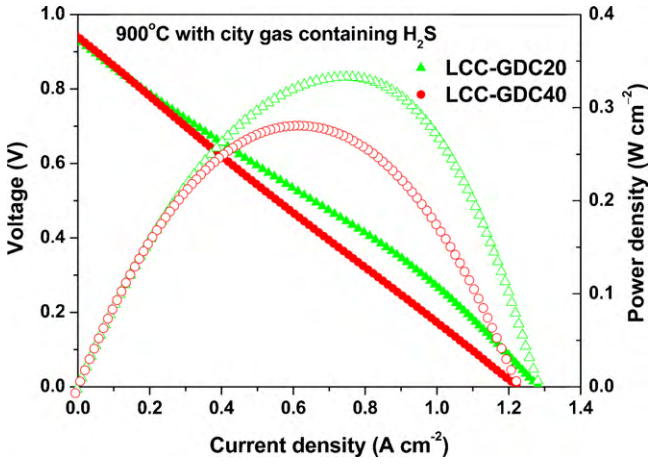

Fig. 7. Voltage and power density as a function of current density for the single-cell with LCC–GDC20 and LCC–GDC40 symmetrical electrodes using the humidified commercial city gas containing H_2S (3% H_2O) as fuel and ambient air as oxidant at 900 °C. Flow rate of the city gas is 50 mL min^{-1}.

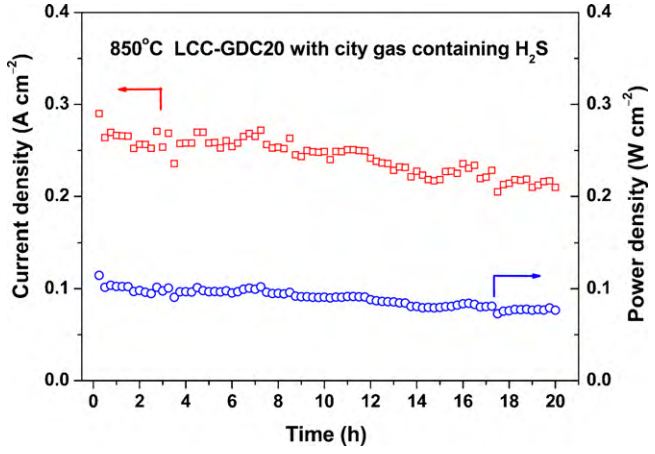

Fig. 8. Electrochemical stability test curve for LCC–GDC20/LSGM/LCC–GDC20 symmetrical cell using the humidified commercial city gas containing H_2S (3% H_2O) as fuel and ambient air as oxidant at 850 °C.

could be a potentially stable anode. In addition, the power density of the cell continuously fluctuated up and down throughout the test period. This could be attributed to the direct use of commercial city gas supplied via the gas main, such that the gas flow was unsteady due to the absence of a pressure-relief device.

SEM and EDS techniques were used to characterize the LCC–GDC40 electrode surfaces after cell testing. Fig. 9(a) and (c) shows the surface morphology of the electrodes after the exposure to H_2 and commercial city gas containing H_2S at 900 °C. No significant differences in the SEM micrographs of electrode surfaces were seen with the effect of exposure to H_2 and city gas containing H_2S. Comparing the surface SEM micrograph of the electrode exposed to city gas containing H_2S with that exposed to H_2, there was no contamination occurring on the electrode surface. Fig. 9(b) and (d) shows the elemental components of the electrodes after the exposure to H_2 and commercial city gas containing H_2S at 900 °C. It can be seen from Fig. 9(b) and (d), the carbon content in the electrode exposed to city gas containing H_2S was very close to that exposed to H_2, suggesting that there is no significant carbon deposition on the electrode after exposure to commercial city gas containing H_2S. Interestingly, no sulfur component was detected by EDS on the electrode surface after exposure to commercial city gas containing H_2S. This was most likely due to GDC being used as catalyst in this study. Zeng et al. [44] reported that the H_2S concentration could be significantly reduced from 10,000 ppm to less than 10 ppm at 850 °C and to near 1 ppm at 700 °C in the product gas when used ceria as sorbent for high-temperature gas desulfurization. And the removal of H_2S to sub-parts per million levels was achieved at very short (millisecond) contact times [45]. Therefore, no sulfur was deposited on the LCC–GDC electrode. The preliminary results indicated that no obvious carbon and sulfur poisoning were observed for the reaction in humidified commercial city gas on LCC–GDC composite anodes. Further studies are needed to assess the long-team stability of performance of SOFCs in city gas containing H_2S.

The maximum power densities of some symmetrical cells with different electrodes and electrolytes under various fuel conditions are summarized in Table 2. Compared with the performances of the symmetrical cells described in the literature, the cells with LCC–GDC electrodes exhibited higher output characteristics. Besides the LSGM electrolyte used, the composite electrodes provided percolation paths for electrons, oxygen ions, and gas;

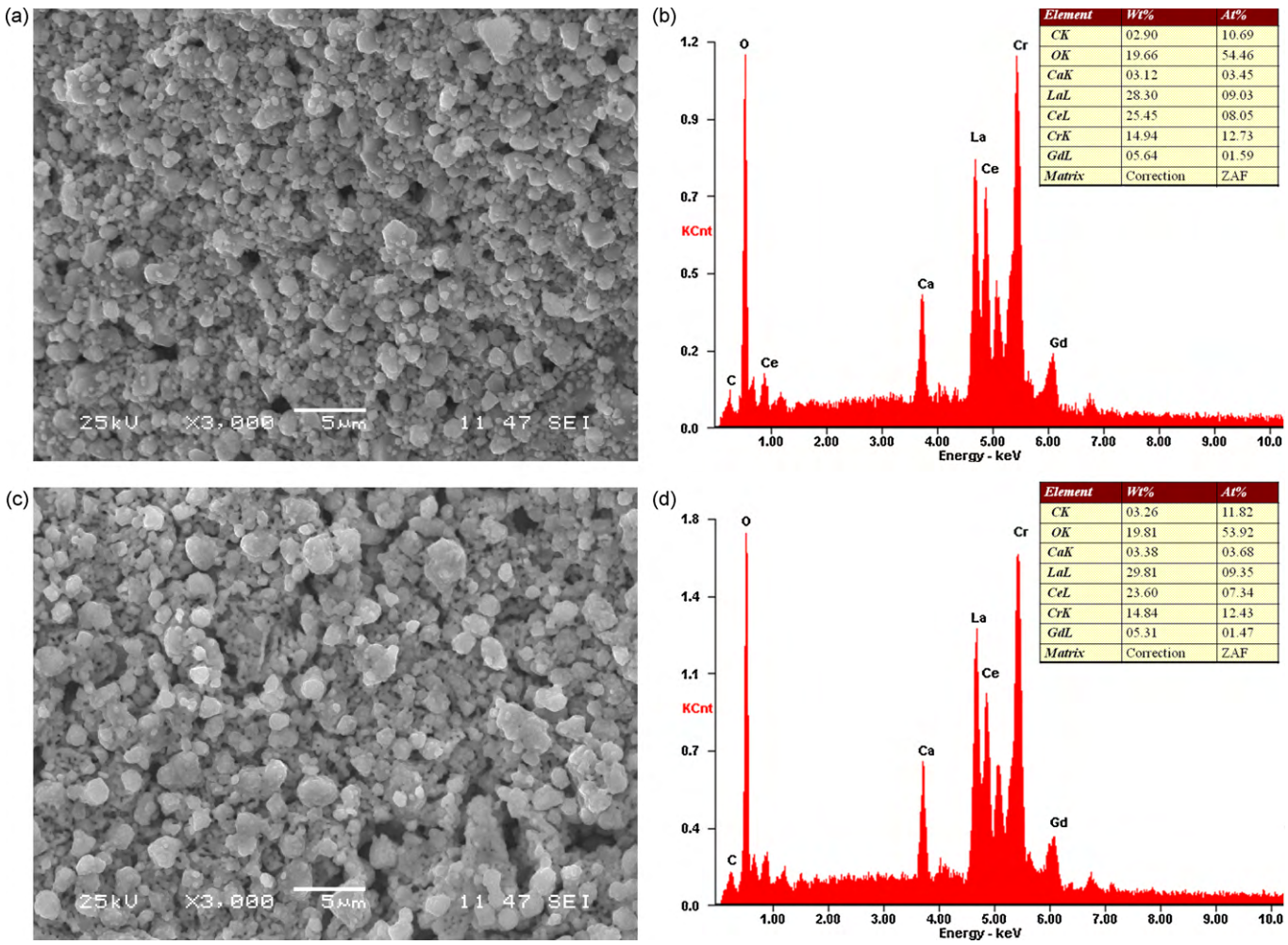

Fig. 9. SEM micrographs and EDS spectra of the LCC–GDC40 electrode surfaces: (a) and (b) after testing in H_2 at 900 °C, and (c) and (d) after testing in the humidified commercial city gas containing H_2S at 900 °C.

improved ionic and electronic conductivities; and promoted oxygen surface exchange, oxygen diffusion, and interfacial transport, thereby resulting in clearly improved performances of the symmetrical cells. Therefore, LCC–GDC could be used as an alternative electrode material in SOFCs.

4. Conclusions

LCC–GDC composites as symmetrical electrodes have been assessed for LSGM electrolyte SOFCs without using an interlayer at the anode/electrolyte interface. LCC displayed good chemical compatibility with GDC and LSGM at temperatures up to 1200 °C. The TECs of the LCC–GDC composites increased from $10.1 \times 10^{-6}\,K^{-1}$ to $10.8 \times 10^{-6}\,K^{-1}$ on increasing the GDC content from 20% to 40%, showing thermal compatibility with the LSGM electrolyte in the temperature range 30–1000 °C. The LCC–GDC20 sample displayed the highest electrical conductivities of $18.64\,S\,cm^{-1}$ in air and $1.86\,S\,cm^{-1}$ in H_2 at 850 °C. Cell performances with the symmetrical electrodes decreased with increasing GDC content due to the decrease in conductivity. The maximum power densities attained with the LCC–GDC/LSGM/LCC–GDC symmetrical cells were 573, 481, and $476\,mW\,cm^{-2}$ at 900 °C in H_2 fuel with GDC contents of 20%, 30%, and 40%, respectively. For the LCC–GDC20/LSGM/LCC–GDC20 cell, a maximum power density of $333\,mW\,cm^{-2}$ at 900 °C was achieved using humidified commercial city gas containing H_2S (3% H_2O). No obvious carbon deposition and sulfur poisoning were observed in city gas over a period of 20 h. The LCC–GDC20 composite showed high electrical conductivity, good thermal expansion compatibility with LSGM electrolyte, and pertinent electrochemical performance, hence it is recommended as a promising symmetrical electrode material for use in SOFCs.

Acknowledgement

This work was supported by the Natural Science Foundation of China under contract no. 10974065.

References

[1] A. Evans, A. Bieberle-Htter, J.L.M. Rupp, L.J. Gauckler, J. Power Sources 194 (2009) 119–129.
[2] V.T. Srikar, K.T. Turner, T.Y.A. Ie, S.M. Spearing, J. Power Sources 125 (2004) 62–69.
[3] J.C. Ruiz-Morales, J. Canales-Vázquez, B. Ballesteros-Pérez, J. Peña-Martínez, D. Marrero-López, J.T.S. Irvine, P. Núñez, J. Eur. Ceram. Soc. 27 (2007) 4223–4227.
[4] J.C. Ruiz-Moralea, J. Canales-Vázquez, D. Marrero-López, D. Pérez-Coll, J. Peña-Martínez, P. Núñez, J. Power Sources 177 (2008) 154–160.
[5] D.M. Bastidas, S. Tao, J.T.S. Irvine, J. Mater. Chem. 16 (2006) 1603–1605.
[6] J.C. Ruiz-Morales, J. Canales-Vázquez, J. Peña-Martínez, D. Marrero-López, P. Núñez, Electrochim. Acta 52 (2006) 278–284.
[7] S.P. Jiang, L. Zhang, Y. Zhang, J. Mater. Chem. 17 (2007) 2627–2635.
[8] Y. Zheng, C. Zhang, R. Ran, R. Cai, Z. Shao, D. Farrusseng, Acta Mater. 57 (2009) 1165–1175.
[9] J.C. Ruiz-Morales, J. Canales-Vázquez, H. Lincke, J. Peña-Martínez, D. Marrero-López, D. Pérez-Coll, J.T.S. Irvine, P. Núñez, Bol. Soc. Esp. Ceram. V 47 (2008) 183–188.
[10] J.C. Ruiz-Morales, H. Lincke, D. Marrero-López, J. Canales-Vázquez, P. Núñez, Bol. Soc. Esp. Ceram. V 46 (2007) 218–223.

[11] S.P. Jiang, S.H. Chan, J. Mater. Sci. 39 (2004) 4405–4439.
[12] Y. Matsuzaki, I. Yasuda, Solid State Ionics 132 (2000) 261–269.
[13] Y. Zhang, B. Liu, B. Tu, Y. Dong, M. Cheng, Solid State Ionics 176 (2005) 2193–2199.
[14] J.H. Kuo, H.U. Anderson, J. Solid State Chem. 87 (1990) 55–63.
[15] J.H. Kuo, H.U. Anderson, J. Solid State Chem. 83 (1989) 52–60.
[16] P. Vernoux, J. Guindet, M. Kleitz, J. Electrochem. Soc. 145 (1998) 3487–3492.
[17] J. Sfeir, P.A. Buffat, P. Möckli, N. Xanthopoulos, R. Vasquez, H.J. Mathieu, J.V. Herle, K.R. Thampi, J. Catal. 202 (2001) 229–244.
[18] S.P. Jiang, L. Liu, K.P. Ong, P. Wu, J. Li, J. Pu, J. Power Sources 176 (2008) 82–89.
[19] E.V. Tsipis, V.V. Kharton, J. Solid State Electrochem. 12 (2008) 1367–1391.
[20] W.Z. Zhu, S.C. Deevi, Mater. Sci. Eng. A 362 (2003) 228–239.
[21] J. Liu, B.D. Madsen, Z. Ji, S.A. Barnett, Electrochem. Solid State Lett. 5 (2002) A122–A124.
[22] B.C.H. Steele, Nature 400 (1999) 619–621.
[23] T. Horita, H. Kishimoto, K. Yamaji, Y. Xiong, N. Sakai, M.E. Brito, H. Yokokawa, Solid State Ionics 177 (2006) 1941–1948.
[24] K.Q. Huang, R. Tichy, J.B. Goodenough, J. Am. Ceram. Soc. 81 (1998) 2581–2585.
[25] J.F. Xue, Y. Shen, Q.J. Zhou, T.M. He, Y.H. Han, Int. J. Hydrogen Energy 35 (2010) 294–300.
[26] L.G. Cong, T.M. He, Y. Ji, P.F. Guan, Y.L. Huang, W.H. Su, J. Alloys Compd. 348 (2003) 325–331.
[27] Y. Shen, M.N. Liu, T.M. He, S.P. Jiang, J. Am. Ceram. Soc. 92 (2009) 2259–2264.
[28] X. Zhou, F. Deng, M. Zhu, G. Meng, X. Liu, J. Power Sources 164 (2007) 293–299.
[29] N. Sakai, H. Yokokawa, T. Horita, K. Yamaji, Int. J. Appl. Ceram. Technol. 1 (2004) 23–30.
[30] M. Mori, T. Yamamoto, H. Itoh, T. Watanabe, J. Mater. Sci. 32 (1999) 2423–2431.
[31] W.Z. Zhu, S.C. Deevi, Mater. Sci. Eng. A 348 (2003) 227–243.
[32] A. Zuev, L. Singheiser, K. Hilpert, Solid State Ionics 147 (2002) 1–11.
[33] S. Wang, B. Lin, K. Xie, Y. Dong, X. Liu, G. Meng, J. Alloys Compd. 468 (2009) 499–504.
[34] M. Mogensen, T. Lindegaard, U. Hansen, J. Electrochem. Soc. 141 (1994) 2122–2128.
[35] N. Sakai, K. Yamaji, T. Horita, H. Yokokawa, T. Kawada, M. Dokiya, J. Electrochem. Soc. 147 (2000) 3178–3182.
[36] J. Mizusaki, S. Yamauchi, K. Fueki, A. Ishikawa, Solid State Ionics 12 (1984) 119–124.
[37] J. Mizusaki, Y. Mima, S. Yamauchi, K. Fueki, H. Tagawa, J. Solid State Chem. 80 (1989) 102–111.
[38] T.R. Armstrong, J.W. Stevenson, L.R. Pederson, P.E. Raney, J. Electrochem. Soc. 143 (1996) 2919–2925.
[39] I. Yasuda, M. Hishinuma, J. Solid State Chem. 115 (1995) 152–157.
[40] M. Liu, L. Zhao, D. Dong, S. Wang, J. Diwu, X. Liu, G. Meng, J. Power Sources 177 (2008) 451–456.
[41] K. Huang, M. Feng, J.B. Goodenough, J. Am. Ceram. Soc. 81 (1998) 357–362.
[42] B.C.H. Steele, Solid State Ionics 129 (2000) 95–110.
[43] L.L. Zhang, Q.J. Zhou, Q. He, T.M. He, J. Power Sources 195 (2010) 6356–6366.
[44] Y. Zeng, S. Kaytakoglu, D.P. Harrison, Chem. Eng. Sci. 55 (2000) 4893–4900.
[45] M. Flytzani-Stephanopoulos, M. Sakbodin, Z. Wang, Science 312 (2006) 1508–1510.
[46] J. Canales-Vázquez, J.C. Ruiz-Morales, D. Marrero-López, J. Peña-Martínez, P. Núñez, P. Gómez-Romero, J. Power Sources 171 (2007) 552–557.
[47] B. Lin, S. Wang, X. Liu, G. Meng, J. Alloys Compd. 490 (2010) 214–222.
[48] A. El-Himri, D. Marrero-López, J.C. Ruiz-Morales, J. Peña-Martínez, P. Núñez, J. Power Sources 188 (2009) 230–237.